Hindawi
Shock and Vibration
Volume 2018, Article ID 6901423, 15 pages
https://doi.org/10.1155/2018/6901423

Research Article

Dynamic Characteristics Analysis of Vehicle Incorporating Hydraulically Interconnected Suspension System with Dual Accumulators

Shengzhao Chen,[1] Bangji Zhang,[1] Boyuan Li,[1,2] and Nong Zhang[3]

[1]*State Key Laboratory of Advanced Design and Manufacture for Vehicle Body, Hunan University, Changsha 410082, China*
[2]*School of Electrical, Computer and Telecommunications Engineering (SECTE), Wollongong, NSW 2522, Australia*
[3]*Automotive Research Institute, Hefei University of Technology, Hefei 230009, China*

Correspondence should be addressed to Bangji Zhang; bangjizhang@126.com

Received 10 April 2018; Accepted 5 July 2018; Published 1 August 2018

Academic Editor: Mario Terzo

A novel roll-resistant hydraulically interconnected suspension with dual accumulators on each fluid circuit (DHIS) is proposed and dynamic characteristics of vehicle incorporating DHIS subsystem are studied in this paper. A 10-degrees-of-freedom (DOFs) vehicle model coupled with DHIS subsystem is established and validated. Four physical parameters of DHIS subsystems which are crucial to vehicle responses are selected with prescribed variation ranges to explore their relationships with the vehicle performance. Simulations of vehicle conducting sine-wave steering maneuvers are carried out to evaluate handling performance with roll angle and vertical tyre force for DHIS subsystem with the parameters varying, compared with the results for vehicle with the original spring-damper suspension and conventional hydraulically interconnected suspension (HIS). On the other hand, ride comfort performance indicated by total weighted root mean square accelerations at the center of gravity is studied when vehicle is excited by three different types of road pavements when the four parameters vary in the prescribed ranges. Simulation results are compared to investigate the special merits of DHIS subsystem, and the parameters that influence the handling performance and ride comfort most are identified. Overall, the DHIS subsystem can effectively enhance the vehicle handling performance compared with the original spring-damper suspension, and it can also benefit much to the ride comfort in contrast to the HIS subsystem.

1. Introduction

Vehicle rollover is the leading cause of fatalities in road crashes. According to the statistics of National Highway Traffic Safety Administration (NHTSA), 33% of all deaths from passenger vehicle crashes are related to rollover accidents in 2002. As a consequence, research studies on suspension system aiming at improving handling performance and reducing rollover propensity has found prosperity in terms of both active/semiactive controlled and passive suspensions [1–8]. Many active/semiactive control strategies, such as H_∞ control strategies and sliding-mode control strategies, have been utilized onto vehicle to enhance handling performance and ride comfort [9–16]. However, they are too expensive for ordinary passenger cars. Therefore, some inexpensive passive suspension systems, which can also benefit vehicle dynamic performance, have been widely studied, such as hydraulic suspension subsystems, to investigate their effects on vehicle dynamics [17, 18].

A large number of researches have been focused on the hydraulic suspension subsystems. Moulton and Best introduced a hydroelastic suspension system, consisting of four hydroelastic units, which are connected in the pitch plane by pipes [19]. Félez and Vera applied the bond-graph method for the design of hydropneumatic suspension [20]. El-Demerdash and Crolla studied the slow active control strategy of hydropneumatic suspension on quarter vehicle model with a previewed road profile [21]. Els and Grobbelaar studied the effects of heat transfer on the spring characteristics of hydropneumatic suspension [22]. Schumann and Anderson utilized the hydragas suspension to improve vehicle ride performance on off-road [23]. Sridhar and Sekar

applied the hydrogas suspension onto tracked vehicle to suit for many different road profiles [24]. Solomon and Padmanabhan applied the skyhook control theory to improve ride performance of a tracked vehicle [25, 26].

The researches above mainly discussed the hydraulic suspension subsystems with independent spring and damping units on vehicle performances. However, the hydraulic suspension with spring and damping effects integrated into one chamber has barely been investigated. Cao et al. proposed this novel type of hydraulic suspension, with each oil chamber employing a gas chamber to adjust the spring effects and with two valves, namely, compression and rebound valves, to adjust the damping effects [27, 28]. In 2010, Cao et al. studied a number of interconnection patterns of hydropneumatic suspension in full-vehicle scale, aiming at finding appropriate fluidic couplings to enhance roll- and pitch-mode stiffness and damping effects, but simultaneously have little effects on bounce- and warp-mode properties [17]. Later on Cao et al. studied the dynamic responses of vehicle with X-shaped hydropneumatic suspension system in the situation of braking-in-a-turn maneuver [29].

Abovementioned researches have studied many types of hydraulic suspensions and their improvements, mainly focused on the utilization on heavy trucks, which take the handling performance and load-bearing capacity as the principal considerations in the design procedure. However, hydraulic suspensions can also be utilized on light vehicles with the emphases mainly on improvement of handling performance at the same time giving more consideration on ride comfort. Different from the hydraulic suspensions mentioned above, hydraulically interconnected suspension (HIS) system does not necessarily remove or replace the original spring-damper suspension system, but works as an auxiliary device to benefit vehicle performances. Zhang et al. took an investigation on the background and modeling of HIS subsystem and introduced a novel type of hydraulic suspension, with all the chambers interconnected with two oil circuits, for the purpose of improving roll motion performance [30]. Smith et al. studied the characteristics of handling performances with fishhook steering input and half-sine bump input [19]. Ding et al. extended the application of HIS subsystem on vehicle with two axles to that with three axles, using the transfer matrix method to generate the final dynamic equations of HIS subsystem [31]. Wang and coworkers developed a motion-mode energy method to identify the contribution of HIS subsystem on vehicle motion modes, which could be used to decouple vehicle dynamic energy distribution on each motion mode [32]. Ding et al. investigated characteristics of the pitch-plane HIS subsystem on two-axle vehicles to formulate feasible regions for subsystem parameters [33]. Liang et al. introduced an interval analysis method for uncertain-but-bounded parameters of HIS subsystem to investigate the influences of uncertain parameters on vehicle's dynamic responses [34].

However, literatures above mainly focused the vehicle characteristics with only one accumulator on each fluidic circuit in HIS subsystem and barely discussed HIS subsystem with dual accumulators on each fluidic circuit. However, DHIS subsystem possesses its own distinctive characteristics comparing with conventional HIS subsystem, such as providing much wider ranges for stiffness and damping adjustment, and alterations of stiffness and damping properties in each mode motion with the help of the variable damping valves adjacent to the additional accumulators. Consequently, a novel DHIS subsystem in roll plane is presented in this paper. The characteristics of DHIS subsystem are numerically investigated in terms of some physical parameters, such as precharged oil pressure, damping coefficients, chamber section area difference, and ratio in the cylinders at front axle.

The rest of the paper will be arranged as follows: Section 2 presents the modeling of vehicle coupled with DHIS in roll plane; in Section 3, the validation of the newly established model will be shown; Section 4 illustrates the relationships between the vehicle dynamic performances and four key physical parameters; and finally, Section 5 concludes the main results.

2. Modeling of Vehicle with DHIS Subsystem

As the DHIS subsystem is working together with the entire spring-damper suspension system in this paper, a 10-DOFs vehicle model is firstly established, for the sake of conducting steering maneuvers and random pavement excitations, simultaneously. The DHIS subsystem, considering the co-actions of the two accumulators in each circuit on oil pressure variations, has been constructed. Consequently, the analytical model of vehicle with DHIS subsystem is presented.

2.1. Vehicle with Original Suspension. As shown in Figure 1, the vehicle model consists of 10-DOFs, including longitudinal, lateral, and vertical displacements at CG, namely, x_s, y_s, and z_s, respectively; roll, pitch, and yaw angles at CG, namely, ϕ, θ, and ψ, respectively; and the vertical displacements z_{ui} ($i = 1, 2, 3, 4$) and rotating angles ϑ_{ui} of four tyres, where the subscript $i = 1, 2, 3$, and 4 correspond to the left-front, right-front, left-rear, and right-rear stations, respectively. The physical parameters of vehicle are listed in Table 1.

In Figure 1, the longitudinal and lateral equations can be obtained with Newton's second law:

$$\begin{aligned}
&\left(m_s + 2m_{uf} + 2m_{ur}\right)\left(\dot{u} - v\dot{\psi}\right) + m_s h_{os}\ddot{\theta} + m_s h_{os}\dot{\phi}\dot{\psi} \\
&\quad - 2\left(m_{uf} l_f - m_{ur} l_r\right)\dot{\psi}^2 = \sum_{i=1\sim 4} F_{xui}, \\
&\left(m_s + 2m_{uf} + 2m_{ur}\right)\left(\dot{v} + u\dot{\psi}\right) - m_s h_{os}\ddot{\phi} - m_s h_{os}\dot{\theta}\dot{\psi} \\
&\quad + 2\left(m_{uf} l_f - m_{ur} l_r\right)\ddot{\psi} = \sum_{i=1\sim 4} F_{yui},
\end{aligned} \tag{1}$$

where m_s is the sprung mass; m_{ui} ($i = 1, 2, 3, 4$) are the unsprung masses (generally speaking, $m_{u1} = m_{u2} = m_{uf}$, $m_{u3} = m_{u4} = m_{ur}$); x_{ui}, y_{ui} are the longitudinal and lateral displacements of four wheels relative to vehicle coordinate, respectively, which can be obtained through the displacements at CG and the vehicle geometry; z_{ui} are the vertical displacements of four wheels along z-axis; and F_{xti} and F_{yti} are the longitudinal and lateral forces in x and y directions generated by tyre-terrain contact, which can be derived through the following equations:

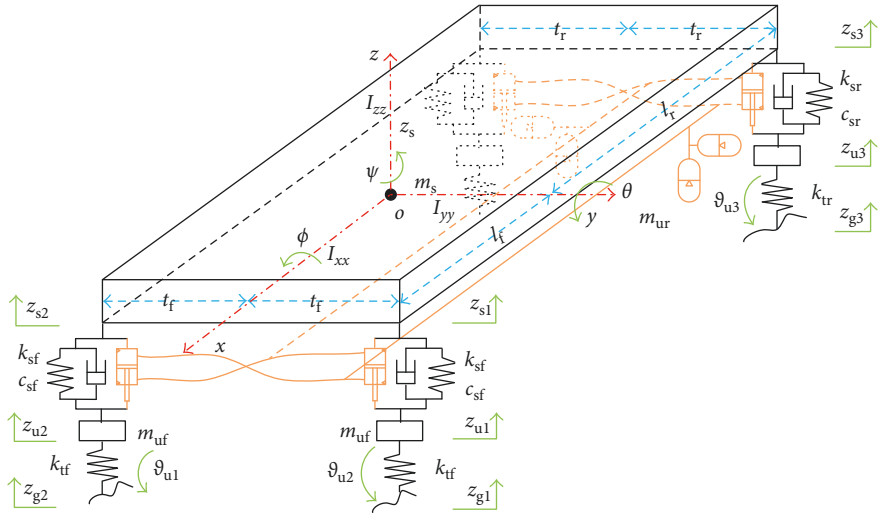

Figure 1: The 10-DOFs vehicle model with DHIS subsystem.

Table 1: Physical parameters of vehicle.

Symbol (unit)	Value	Description
m_s (kg)	1310	Sprung mass
I_{xx} (kg·m^2)	560	Roll inertia of sprung mass
I_{yy} (kg·m^2)	1670	Pitch inertia of sprung mass
I_{zz} (kg·m^2)	2370	Yaw inertia of vehicle
m_{uf} (kg)	63	Unsprung mass in front axle
m_{ur} (kg)	57	Unsprung mass in rear axle
I_{uyy} (kg·m^2)	10	Rotation inertia of tyre
c_{sf} (N·s·m^{-1})	2000	Damping coefficient of front suspension
c_{sr} (N·s·m^{-1}	2200	Damping coefficient of rear suspension
k_{sf} (N·m^{-1})	36000	Spring stiffness of front suspension
k_{sr} (N·m^{-1})	39000	Spring stiffness of rear suspension
c_{tf} (N·s·m^{-1})	100	Damping coefficient of front tyre
c_{tr} (N·s·m^{-1})	100	Damping coefficient of rear tyre
k_{tf} (N·m^{-1})	240000	Front tyre stiffness
k_{tr} (N·m^{-1})	240000	Rear tyre stiffness
l_f (m)	1.15	Length from CG to front axle
l_r (m)	1.53	Length from CG to rear axle
t_f (m)	0.78	Half-track width in front axle
t_r (m)	0.78	Half-track width in rear axle
h_{os} (m)	0.43	Height from vehicle rolling center to CG of sprung mass
h_{oc} (m)	0.11	Height from vehicle rolling center to chassis bottom
i_{sw} (1)	25.0	Steering ratio

$$\begin{aligned} F_{xti} &= F_{txi}\cos\delta_{ui} - F_{tyi}\sin\delta_{ui}, \\ F_{yti} &= F_{txi}\sin\delta_{ui} + F_{tyi}\cos\delta_{ui}, \end{aligned} \tag{2}$$

where F_{txi} and F_{tyi} are the contact forces in tyre coordinates generated with DUGOFF tyre model [35] and δ_{ui} are tyre steering angles.

Meanwhile, the dynamic equation at z-axis for sprung mass can be derived as

$$m_s\ddot{z}_s = -\sum_{i=1}^{4} F_{zsi}, \tag{3}$$

where F_{zsi} are the suspension forces imposed on sprung mass along z-axis. F_{zsi} can be derived with suspension deflections and their derivatives as follows:

$$F_{zsi} = k_{si}(z_{si} - z_{ui}) + c_{si}(\dot{z}_{si} - \dot{z}_{ui}), \tag{4}$$

where z_{si} are z-axis displacements of the sprung mass at four suspension stations. z_{si} can be obtained through the state variables of sprung mass and the suspension geometry as

$$\begin{bmatrix} z_{s1} \\ z_{s2} \\ z_{s3} \\ z_{s4} \end{bmatrix} = \begin{bmatrix} 1 & +t_f & -l_f \\ 1 & -t_f & -l_f \\ 1 & +t_r & +l_r \\ 1 & -t_r & +l_r \end{bmatrix} \begin{bmatrix} z_s \\ \phi \\ \theta \end{bmatrix}, \tag{5}$$

where l_f and l_r are the length from CG to the front and rear axles, respectively, and t_f and t_r are the half-track width of the front and rear axles, respectively.

Similarly, the momentum equations along x-axis and y-axis for sprung mass can be formulated as

$$I_{xx}\ddot{\phi} + (I_{zz} - I_{yy})\dot{\theta}\dot{\psi} = \sum_{i=1}^{4} M_{xri}, \tag{6}$$

$$I_{yy}\ddot{\theta} + (I_{xx} - I_{zz})\dot{\phi}\dot{\psi} = \sum_{i=1}^{4} M_{yri}, \tag{7}$$

where I_{xx} and I_{yy} are the rotary inertia along x-axis and y-axis of sprung mass and M_{xri} and M_{yri} are the x-axis and y-axis momentums imposed by unsprung mass onto sprung mass, respectively. The summations of M_{xri} and M_{yri} can be obtained as follows:

$$\begin{aligned}\sum_{i=1}^{4} M_{xri} &= -\left(t_f F_{zs1} - t_f F_{zs2} + t_r F_{zs3} - t_r F_{zs4}\right) \\ &\quad - h_{oc}\left(F_{yt1} + F_{yt2}\right) - h_{oc}\left(F_{yt3} + F_{yt4}\right), \\ \sum_{i=1}^{4} M_{yri} &= -\left(-l_f F_{zs1} - l_f F_{zs2} + l_r F_{zs3} + l_r F_{zs4}\right) \\ &\quad + h_{oc}\left(F_{xt1} + F_{xt2}\right) + h_{oc}\left(+F_{xt3} + F_{xt4}\right),\end{aligned} \tag{8}$$

where h_{oc} is the height from the vehicle body rolling center to the chassis bottom.

The momentum equation for vehicle in z-plane can be obtained as follows:

$$\begin{aligned}&I_{zz}\ddot{\psi} + 2\left(m_{uf}\left(l_f^2 + t_f^2\right) + m_{ur}\left(l_r^2 + t_r^2\right)\right)\ddot{\psi} \\ &\quad + \left(I_{yy} - I_{xx}\right)\dot{\phi}\dot{\theta} = \sum_{i=1}^{4} M_{zri},\end{aligned} \tag{9}$$

where I_{zz} is the rotary inertia of the vehicle along z-axis and M_{zri} is the z-axis momentum imposed by tyre-terrain contact onto vehicle. The summation of M_{zri} can be obtained by the following equation:

$$\begin{aligned}\sum_{i=1}^{4} M_{zri} &= \left(l_f F_{yt1} + l_f F_{yt2} - l_r F_{yt3} - l_r F_{yt4}\right) \\ &\quad + \left(-t_f F_{xt1} + t_f F_{xt2} - t_r F_{xt3} + t_r F_{xt4}\right) + \sum_{i=1}^{4} M_{tzi},\end{aligned} \tag{10}$$

where M_{tzi} are the self-aligning momentums of tyres.

The z-axis force balance equations for unsprung masses can be formulated as follows:

$$F_{zsi} = m_{ui}\ddot{z}_{ui} + c_{ti}\left(\dot{z}_{ui} - \dot{z}_{gi}\right) + k_{ti}\left(z_{ui} - z_{gi}\right), \tag{11}$$

where c_{ti} and K_{ti} are the damping and stiffness coefficients of tyres, respectively, and z_{gi} are the road pavement excitations at each tyre.

Based on the above analysis, the integrated vehicle model can be formulated as follows:

$$\begin{aligned}&\begin{bmatrix}\mathbf{M}_w & \mathbf{0} & \mathbf{0} \\ \mathbf{0} & \mathbf{M}_s & \mathbf{0} \\ \mathbf{0} & \mathbf{0} & \mathbf{M}_u\end{bmatrix}\begin{bmatrix}\ddot{\mathbf{X}}_w \\ \ddot{\mathbf{X}}_s \\ \ddot{\mathbf{Z}}_u\end{bmatrix} + \begin{bmatrix}\mathbf{C}_w & \mathbf{0} & \mathbf{0} \\ \mathbf{0} & \mathbf{T}_s^T\mathbf{C}_s\mathbf{T}_s & -\mathbf{T}_s^T\mathbf{C}_s \\ \mathbf{0} & -\mathbf{C}_s\mathbf{T}_s & \mathbf{C}_s + \mathbf{C}_t\end{bmatrix}\begin{bmatrix}\dot{\mathbf{X}}_w \\ \dot{\mathbf{X}}_s \\ \dot{\mathbf{Z}}_u\end{bmatrix} \\ &\quad + \begin{bmatrix}\mathbf{0} & \mathbf{0} & \mathbf{0} \\ \mathbf{0} & \mathbf{T}_s^T\mathbf{K}_s\mathbf{T}_s & -\mathbf{T}_s^T\mathbf{K}_s \\ \mathbf{0} & -\mathbf{K}_s\mathbf{T}_s & \mathbf{K}_s + \mathbf{K}_t\end{bmatrix}\begin{bmatrix}\mathbf{X}_w \\ \mathbf{X}_s \\ \mathbf{Z}_u\end{bmatrix} = \begin{bmatrix}\mathbf{W} \\ \mathbf{R} \\ \mathbf{C}_t\dot{\mathbf{Z}}_g + \mathbf{K}_t\mathbf{Z}_g\end{bmatrix},\end{aligned} \tag{12}$$

where $\mathbf{X}_w = [x_s, y_s, \psi]^T$, $\mathbf{X}_s = [z_s, \phi, \theta]^T$, $\mathbf{Z}_u = [z_{u1}, z_{u2}, z_{u3}, z_{u4}]^T$, $\mathbf{M}_s = \mathrm{diag}([m_s, I_{xx}, I_{yy}])$, $\mathbf{M}_u = \mathrm{diag}([m_{u1}, m_{u2}, m_{u3}, m_{u4}])$, $C_s = \mathrm{diag}([c_{sf}, c_{sf}, c_{sr}, c_{sr}])$, $\mathbf{K}_s = \mathrm{diag}([k_{sf}, k_{sf}, k_{sr}, k_{sr}])$, $\mathbf{C}_t = \mathrm{diag}([c_{tf}, c_{tf}, c_{tr}, c_{tr}])$, $\mathbf{K}_t = \mathrm{diag}([k_{tf}, k_{tf}, k_{tr}, k_{tr}])$, $\mathbf{0}$ denotes the zero matrix of proper dimensions, and

$$\begin{aligned}\mathbf{M}_w &= \begin{bmatrix}m_s + 2m_{uf} + 2m_{ur} & 0 & 0 \\ 0 & m_s + 2m_{uf} + 2m_{ur} & 0 \\ 0 & 0 & I_{zz} + 2m_{uf}\left(l_f^2 + t_f^2\right) + 2m_{ur}\left(l_r^2 + t_r^2\right)\end{bmatrix} \\ \mathbf{C}_w &= \begin{bmatrix}0 & -\left(m_s + 2m_{uf} + 2m_{ur}\right)\dot{\psi} & 0 \\ +\left(m_s + 2m_{uf} + 2m_{ur}\right)\dot{\psi} & 0 & 0 \\ 0 & 0 & 0\end{bmatrix} \\ \mathbf{W} &= \begin{bmatrix}\sum_{i=1\sim4} F_{xui} - m_s h_{os}\ddot{\theta} - m_s h_{os}\dot{\phi}\dot{\psi} + 2\left(m_{uf}l_f - m_{ur}l_r\right)\dot{\psi}^2 \\ \sum_{i=1\sim4} F_{yui} + m_s h_{os}\ddot{\phi} + m_s h_{os}\dot{\theta}\dot{\psi} - 2\left(m_{uf}l_f - m_{ur}l_r\right)\ddot{\psi} \\ \sum_{i=1}^{4} M_{zri} - \left(I_{yy} - I_{xx}\right)\dot{\phi}\dot{\theta}\end{bmatrix} \\ \mathbf{T}_s &= \begin{bmatrix}1 & +t_f & -l_f \\ 1 & -t_f & -l_f \\ 1 & +t_r & +l_r \\ 1 & -t_r & +l_r\end{bmatrix}, \\ \mathbf{R} &= \begin{bmatrix}0 \\ -h_{oc}\sum_{i=1}^{4} F_{yti} - \left(I_{zz} - I_{yy}\right)\dot{\theta}\dot{\psi} \\ +h_{oc}\sum_{i=1}^{4} F_{xti} - \left(I_{xx} - I_{zz}\right)\dot{\phi}\dot{\psi}\end{bmatrix}\end{aligned} \tag{13}$$

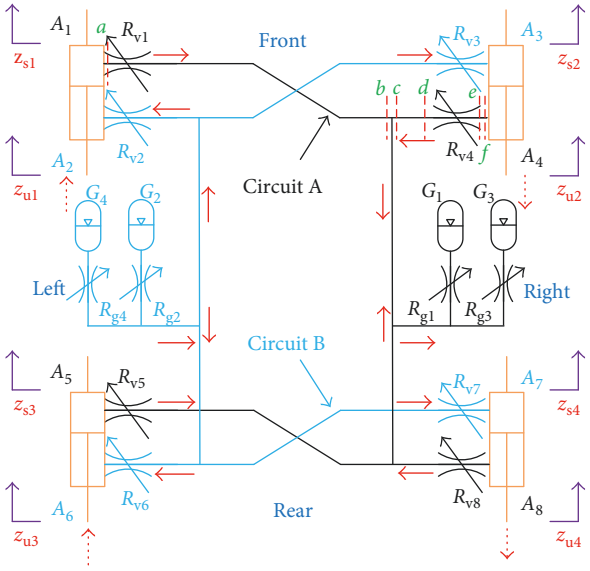

Figure 2: The diagram of roll plane DHIS subsystem.

2.2. DHIS Subsystem. The DHIS subsystem is designed in the roll plane, as shown in Figure 2, and its physical parameters are listed in Table 2. When the vehicle performs steering maneuvers, without loss of generality, the fact that the cylinders and pistons are moving relatively can be equivalent to the process that only the pistons are traveling in the comprehensive movements while the cylinders are fixed, as the red dashed arrows shown in the figure. Consequently, the fluid in the chambers is flowing in and out as depicted with red solid arrows in the figure, where the line thickness represents the flow quantity relatively. It can be seen clearly from these arrows that a large quantity of fluid flows into the accumulators in Circuit A, but contrary for Circuit B. Eventually, oil pressure in A rises while that in B goes down, which means, the oil pressures in each chamber are changed. Consequently, the DHIS subsystem generates a roll-resistant torque to retard further roll motion.

In DHIS subsystem, the upper chambers of cylinders are connected with vehicle body, and lower chambers are connected with unsprung masses, as shown in Figure 2. Therefore, the displacements z_{si} $(i = 1, 2, 3, 4)$ of upper cylinders are the same as those in the joints on vehicle body. Then, the oil volume variations in upper chambers $\Delta V_{\mathrm{Ht}i}$ and lower chambers $\Delta V_{\mathrm{Hb}i}$ can be obtained as follows:

$$\begin{aligned} \Delta V_{\mathrm{Ht}i} &= A_{\mathrm{t}i}\left(z_{si} - z_{\mathrm{u}i}\right), \\ \Delta V_{\mathrm{Hb}i} &= -A_{\mathrm{b}i}\left(z_{si} - z_{\mathrm{u}i}\right). \end{aligned} \tag{14}$$

The oil pressure loss through the damper valves can be expressed as

$$\Delta p_{\mathrm{v}i} = R_{\mathrm{v}i} Q_{\mathrm{v}i}, \tag{15}$$

where the fluid quantity at the valves adjacent to the upper and lower inlets/outlets of hydraulic cylinders can be expressed as $Q_{\mathrm{v}i} = A_{\mathrm{t}i}\left(\dot{z}_{si} - \dot{z}_{\mathrm{u}i}\right)$ or $Q_{\mathrm{v}i} = A_{\mathrm{b}i}\left(\dot{z}_{si} - \dot{z}_{\mathrm{u}i}\right)$.

Table 2: Physical parameters of DHIS subsystem.

Symbol (unit)	Value	Description
p_0 (Pa)	2.0×10^6	Precharged oil pressure
V_{10} (L)	0.35	Precharged gas volume in accumulator
V_{20} (L)	0.30	Precharged gas volume in accumulator
A_{ft} (m^2)	0.0016	Cross area of front-top chamber
A_{fb} (m^2)	0.0012	Cross area of front-bottom chamber
A_{rt} (m^2)	0.0016	Cross area of rear-top chamber
A_{rb} (m^2)	0.0012	Cross area of rear-bottom chamber
R_{vf} ($\mathrm{kg{\cdot}s^{-1}{\cdot}m^{-4}}$)	0.16×10^8	Damping coefficient of front valves
R_{vr} ($\mathrm{kg{\cdot}s^{-1}{\cdot}m^{-4}}$)	0.16×10^8	Damping coefficient of rear valves
$R_{\mathrm{g}1}/R_{\mathrm{g}2}$ ($\mathrm{kg{\cdot}s^{-1}{\cdot}m^{-4}}$)	1.0×10^8	Damping coefficient of valves adjacent to the accumulators G_1/G_2
$R_{\mathrm{g}3}/R_{\mathrm{g}4}$ ($\mathrm{kg{\cdot}s^{-1}{\cdot}m^{-4}}$)	1.0×10^8	Damping coefficient of valves adjacent to the accumulators G_3/G_4

Take Circuit A, for instance, define ΔV_{A} as the total oil volume flowing into the two accumulators G_1 and G_3, and define $\Delta V_{\mathrm{A}1}$ and $\Delta V_{\mathrm{A}3}$ as the oil volumes flowing into accumulators G_1 and G_3, respectively. Then, the following equations can be obtained through the properties of accumulators and fluid:

$$\begin{aligned} \Delta V_{\mathrm{A}} &= \sum_{i=1,3} \Delta V_{\mathrm{Ht}i} + \sum_{j=2,4} \Delta V_{\mathrm{Hb}j}, \\ \Delta V_{\mathrm{A}} &= \Delta V_{\mathrm{A}1} + \Delta V_{\mathrm{A}3}, \\ \Delta p_{\mathrm{g}1} &= R_{\mathrm{g}3} \Delta \dot{V}_{\mathrm{A}3}, \\ p_{\mathrm{g}1} &= p_0 \left(1 - \frac{\Delta V_{\mathrm{A}1}}{V_{10}}\right)^{-\gamma}, \\ p_{\mathrm{g}3} &= p_0 \left(1 - \frac{\Delta V_{\mathrm{A}3}}{V_{20}}\right)^{-\gamma}, \\ p_{\mathrm{g}1} &= p_{\mathrm{g}3} + \Delta p_{\mathrm{g}1}, \end{aligned} \tag{16}$$

where $\Delta \dot{V}_{\mathrm{A}3}$ is the derivative of $\Delta V_{\mathrm{A}3}$ relative to time t; $R_{\mathrm{g}j}$ $(j = 1, 2, 3, 4)$ are damping coefficients of the valves adjacent to the accumulators G_j; $\Delta p_{\mathrm{g}j}$ are the pressure loss at valve $R_{\mathrm{g}j}$; p_0 is the precharged oil pressure in DHIS subsystem; V_{10} and V_{20} are the precharged gas volumes at G_1/G_2 and G_3/G_4, respectively; and $p_{\mathrm{g}i}$ $(i = 1, 2, 3, 4)$ are the oil pressures at G_i, respectively.

The status in Circuit B can be derived similarly with (16). Then with (15) and (16), the oil pressure at each chamber in DHIS subsystem can be obtained as follows:

$$\mathbf{P}(t) = \mathbf{P}_{\mathrm{g}}(t) - \Delta \mathbf{P}_{\mathrm{g}}(t) - \Delta \mathbf{P}_{\mathrm{v}}(t), \tag{17}$$

where $\mathbf{P}(t) = [p_{t1}, p_{b1}, p_{t2}, p_{b2}, p_{t3}, p_{b3}, p_{t4}, p_{b4};]^T$, $\mathbf{P}_g(t) = [p_{g1}, p_{g2}, p_{g2}, p_{g1}, p_{g1}, p_{g2}, p_{g2}, p_{g1};]^T$, $\Delta\mathbf{P}_g(t) = [\Delta p_{g1}, \Delta p_{g2}, \Delta p_{g2}, \Delta p_{g1}, \Delta p_{g1}, \Delta p_{g2}, \Delta p_{g2}, \Delta p_{g1};]^T$, $\Delta\mathbf{P}_v(t) = [\Delta p_{v1}, \Delta p_{v2}, \Delta p_{v3}, \Delta p_{v4}, \Delta p_{v5}, \Delta p_{v6}, \Delta p_{v7}, \Delta p_{v8};]^T$, where Δp_{vi} $(i = 1, 2, \ldots, 8)$ are the pressure loss at R_{vi}. Both Δp_{gi} and Δp_{vi} can be obtained with (15).

Then forces generated by DHIS subsystem acting on vehicle body in z-axis can be expressed as follows:

$$\mathbf{F}_{Hs}(t) = \mathbf{T}_{\mathbf{F}\leftarrow\mathbf{P}}\mathbf{P}(t), \tag{18}$$

where $\mathbf{T}_{\mathbf{F}\leftarrow\mathbf{P}}$ is the state transfer matrix from oil pressures to acting forces, namely,

$$\mathbf{T}_{\mathbf{F}\leftarrow\mathbf{P}} = \begin{bmatrix} A_{1t} & -A_{1b} & 0 & 0 & 0 & 0 & 0 & 0 \\ 0 & 0 & A_{2t} & -A_{2b} & 0 & 0 & 0 & 0 \\ 0 & 0 & 0 & 0 & A_{3t} & -A_{3b} & 0 & 0 \\ 0 & 0 & 0 & 0 & 0 & 0 & A_{4t} & -A_{4b} \end{bmatrix}. \tag{19}$$

Considering the vehicle geometry and the vertical forces (18), forces acting on vehicle system can be expressed as follows:

$$\mathbf{F}_H(t) = \begin{bmatrix} \mathbf{T}_s^T \\ -\mathbf{I}_{(4\times4)} \end{bmatrix}\mathbf{T}_{\mathbf{F}\leftarrow\mathbf{P}}\mathbf{P}(t). \tag{20}$$

In (20), the first three lines of $\mathbf{F}_H(s)$ are momentums acting on z_s, ϕ, θ, respectively, and the last four lines are forces acting on z_{ui} $(i = 1, 2, 3, 4)$, respectively.

2.3. Vehicle Coupled with DHIS Subsystem. Applying the forces in (20) onto the corresponding vehicle model in (12), the integrated mechanical-hydraulic coupled vehicle model incorporating DHIS subsystem can be rebuilt as follows:

$$\begin{bmatrix} \mathbf{M}_w & \mathbf{0} & \mathbf{0} \\ \mathbf{0} & \mathbf{M}_s & \mathbf{0} \\ \mathbf{0} & \mathbf{0} & \mathbf{M}_u \end{bmatrix}\begin{bmatrix} \ddot{\mathbf{X}}_w \\ \ddot{\mathbf{X}}_s \\ \ddot{\mathbf{Z}}_u \end{bmatrix} + \begin{bmatrix} \mathbf{C}_w & \mathbf{0} & \mathbf{0} \\ \mathbf{0} & \mathbf{T}_s^T\mathbf{C}_s\mathbf{T}_s & -\mathbf{T}_s^T\mathbf{C}_s \\ \mathbf{0} & -\mathbf{C}_s\mathbf{T}_s & \mathbf{C}_s + \mathbf{C}_t \end{bmatrix}\begin{bmatrix} \dot{\mathbf{X}}_w \\ \dot{\mathbf{X}}_s \\ \dot{\mathbf{Z}}_u \end{bmatrix}$$
$$+ \begin{bmatrix} \mathbf{0} & \mathbf{0} & \mathbf{0} \\ \mathbf{0} & \mathbf{T}_s^T\mathbf{K}_s\mathbf{T}_s & -\mathbf{T}_s^T\mathbf{K}_s \\ \mathbf{0} & -\mathbf{K}_s\mathbf{T}_s & \mathbf{K}_s + \mathbf{K}_t \end{bmatrix}\begin{bmatrix} \mathbf{X}_w \\ \mathbf{X}_s \\ \mathbf{Z}_u \end{bmatrix} = \begin{bmatrix} \mathbf{W} \\ \mathbf{R} \\ \mathbf{C}_t\dot{\mathbf{Z}}_g + \mathbf{K}_t\mathbf{Z}_g \end{bmatrix} + \begin{bmatrix} \mathbf{0} \\ \mathbf{F}_H \end{bmatrix}. \tag{21}$$

3. Validation of the Vehicle Model with DHIS Subsystem

The vehicle model with DHIS subsystem will conduct a maneuver, such as sine-wave steering, to verify its effectiveness through result comparisons between MATLAB and CarSim in this section.

In the ensuing simulations, at initial time $t = 0$ s, the vehicle with DHIS subsystem is in static equilibrium with the precharged oil pressure $p_0 = 2.0$ MPa and the precharged gas volumes in G_1/G_2 $V_{10} = 0.35$ L together with that in G_3/G_4 $V_{20} = 0.10$ L. At the next instant, the wheel steering input is implemented to the vehicle model, so the dynamic states of mechanical and hydraulic subsystems are determined by (3), (6), (7), (11), and (20). A fourth-order Runge–Kutta numerical integration method is utilized to solve the dynamic equations.

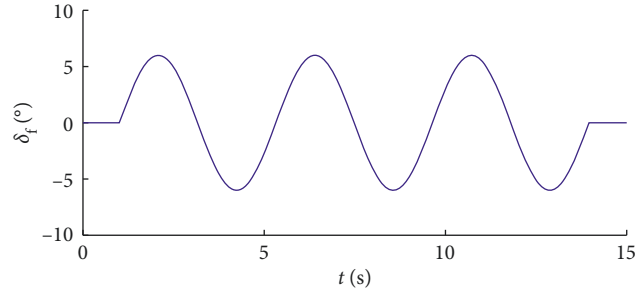

Figure 3: Sine-wave steering angle for front wheels.

The vehicle model is subject to a sine-wave maneuver. Figure 3 shows the wheel steering angle input as a function of time.

The vehicle velocity is set to $v = 50$ km/h. Two vehicle output variables, including roll angle and vertical tyre force in left-front station, are used as the indicators to evaluate vehicle handling performance.

Comparisons of the results from MATLAB and CarSim are shown in Figure 4. It can be seen from the plots that the roll angle and tyre force acquired from MATLAB are slightly larger than the results from CarSim. The main reason for this phenomenon is that some parameters in the two simulation platforms, such as the locations of suspension joints, can hardly be adjusted the same. However, generally speaking, the results from the MATLAB simulations are fitting well enough with those acquired from CarSim. Therefore, the vehicle model with DHIS subsystem established in 2 can be effectively utilized for further analyses.

4. Results and Discussion

In this section, the vehicle performance, including handling performance in time domain and ride performance in frequency domain, is investigated. The physical parameters of DHIS subsystem play significant roles in vehicle dynamic behaviors. Considering the similarity of vehicle responses between front and rear axles, only those parameters in front axle are considered for brevity. Four physical parameters, including the precharged oil pressure p_0 in hydraulic suspension subsystems, the area difference/ratio of hydraulic chambers in front axle ($\Delta A_f/\lambda_{Af}$, namely, $\Delta A_f = A_{1t} - A_{1b} = A_{2t} - A_{2b}$, $\lambda_{Af} = A_{1b}/A_{1t} = A_{2b}/A_{2t}$), and the damping coefficients of R_{g1}/R_{g2}, are chosen as the crucial factors due to their important effects on suspension characteristics, and their variation ranges are prescribed as shown in Table 3.

To observe the differences among vehicle behaviors influenced by suspension system, the results of vehicle with an additional DHIS subsystem (denoted as S-III for brevity) are derived compared with those results of vehicles with the other two types of suspension system: the original spring-damper suspension system (denoted as S-I) and the

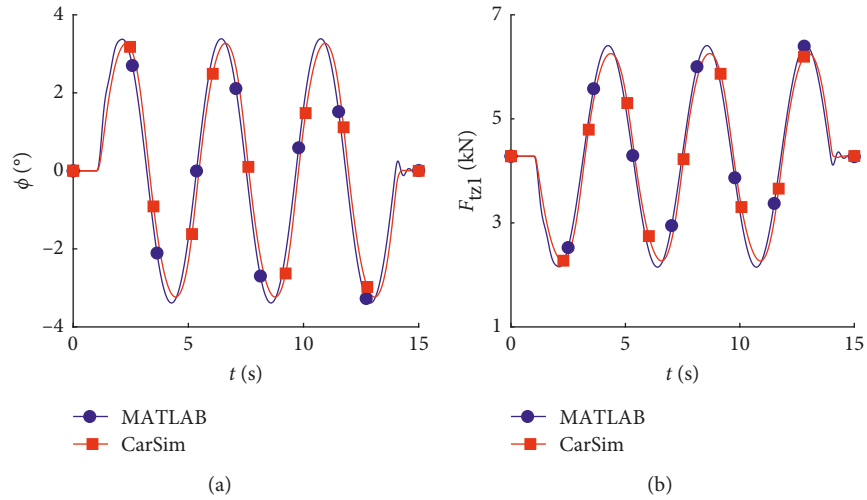

Figure 4: Comparisons of simulation results: (a) roll angle; (b) vertical tyre force at left-front station.

Table 3: Parameter variation ranges of hydraulic suspension subsystems.

Symbol (unit)	Lower limits	Upper limits
p_0 (MPa)	0.0	4.0
ΔA_f ($\times 10^{-4}\cdot m^2$)	1.0	13.0
λ_{Af} (1)	0.1	0.8
R_{g1}/R_{g2} ($\times 10^{8}\cdot kg\cdot m^{-4}\cdot s^{-1}$)	0.0	4.6

suspension system with both the original suspension and HIS subsystem (denoted as S-II).

4.1. Influence of Physical Parameters on Handling Performance. The maneuver with sine-wave steering (Figure 3) is adopted to evaluate the handling performances of vehicle with the three types of suspension system. For brevity, only the responses, including the roll angle ϕ and tyre force in left-front tyre F_{tz1}, are chosen to indicate handling performance. Simulations are carried out to investigate the influence of the four physical parameters on the two responses.

During the simulations, the vehicle runs at a speed of $v = 50$ km/h. The dynamic responses in time domain are depicted in Figure 5.

Figure 5(a) shows that the hydraulic suspension systems (including both DHIS and HIS subsystems) have significantly reduced the amplitudes of roll angle, which means the roll stiffness has been effectively enhanced with hydraulic suspension subsystems. Figure 5(b) shows that the tyre load has been observed significant decreases for vehicle with DHIS and HIS subsystems comparing with vehicle with only the original suspension system, which means the tyre-terrain contact situation has been improved. However, comparing with HIS subsystem, DHIS subsystem has a less stiffened roll motion, which is due to effect of the additional gas accumulators. The DHIS subsystem has provided more gas to soften the suspension stiffness compared with the HIS subsystem.

Analyses above show that the hydraulic suspension subsystems can effectively affect the vehicle performances. However, these effects can be further simplified by choosing the appropriate features of responses. It is obvious that the mean values of roll angle ϕ and tyre force F_{tz1} are constant ($\phi_m = 0$ rad, $F_{tz1m} = 4282$ N, where the subscript "m" denotes the mean value) during the whole simulation processes. However, the amplitudes for the dynamic responses keep varying among the three types of suspension system. Therefore, the amplitude of roll angle ϕ_a and that of tyre force F_{tz1a} are chosen as the features to indicate the handling performances.

4.1.1. Precharged Oil Pressure. Figure 6 shows the characteristics of vehicle responses as the precharged oil pressure p_0 changes. In Figure 6(a), the roll angle decreases as p_0 increases. This phenomenon can be explained that when p_0 goes up, the roll stiffness generated by hydraulic suspension subsystems increases, and thus, roll motion of vehicle is retarded. Therefore, the load transferred from left side to right side which mainly depends on the sprung mass roll motion is reduced, which means the roll holding ability has been enhanced, as shown in Figure 6(b). Although the lateral acceleration can also contribute to the tyre load transfer, but this value hardly changes as the suspension system alters. It can also be observed from Figures 6(a) and 6(b) that the DHIS subsystem produces larger peak values of roll angle and tyre force than the HIS subsystem.

4.1.2. Area Difference in Front Hydraulic Cylinders. Figure 7 shows the characteristics of vehicle responses as the chamber area difference in front axle ΔA_f changes. Figure 7(a) shows that as ΔA_f increases, the roll angle decreases, but as ΔA_f goes larger, such as from 8×10^{-4} m^2 to 13×10^{-4} m^2, the decrease tendency becomes slow. The reason for the downward trend of roll angle amplitude can be explained: the volumes of fluid flowing into the accumulators increase together with the ΔA_f when vehicle performs roll motion, and then the gas pressure, as well as the oil pressure, goes up. Consequently, the vehicle becomes difficult to perform roll motion. In Figure 7(b), the vertical tyre load F_{tz1} shows an upward trend as ΔA_f increases. It can be observed in Figure 7 that the DHIS subsystem produces larger peak values for roll angle and tyre force, but as ΔA_f

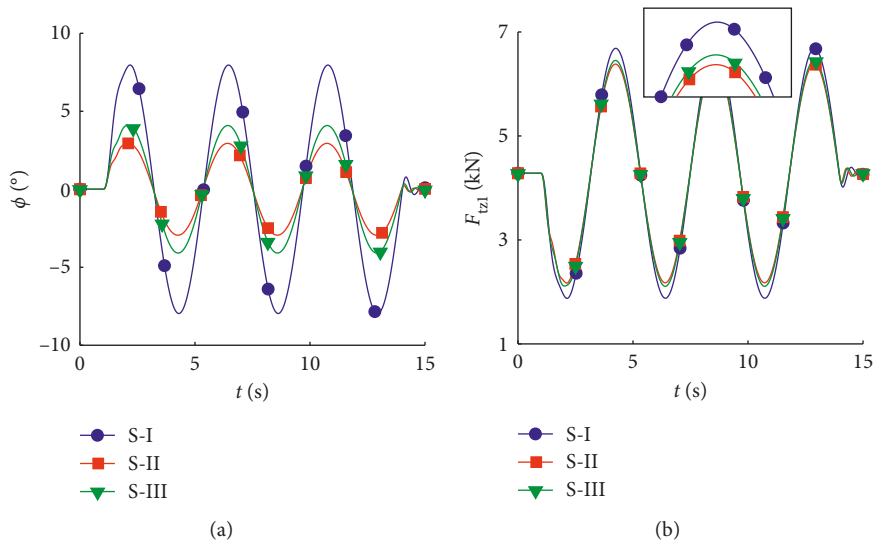

Figure 5: Responses for vehicle with the three types of suspension system: (a) roll angle of sprung mass; (b) vertical tyre force at left-front station.

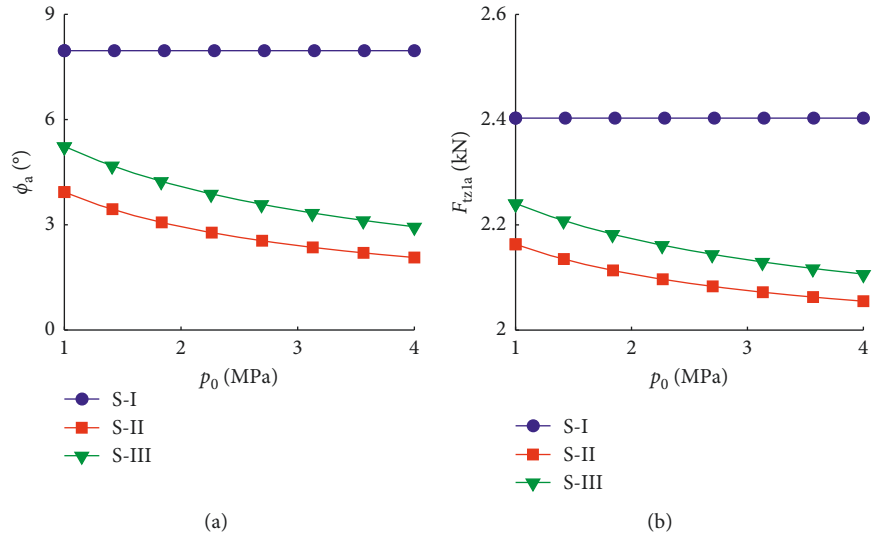

Figure 6: Influence of p_0 on amplitudes of vehicle responses: (a) roll angle of sprung mass; (b) vertical tyre force at left-front station.

increases, the gap between the responses of vehicle with DHIS subsystem and HIS subsystem has been narrowed.

4.1.3. Area Ratio in Front Hydraulic Cylinders. Figure 8 shows the characteristics of vehicle responses as the chamber area ratio λ_{Af} changes. Figure 8(a) shows that as λ_{Af} increases, the roll angle decreases. When λ_{Af} becomes larger, the inner diameter of hydraulic cylinders in front axle goes up. Consequently, the volume of fluid flowing into the accumulators becomes larger than that of the fluid that flowing from the accumulators to the cylinders in rear axle; thus, the gas pressure as well as the oil pressure increases. Therefore, the reason for the decrease of roll angle can be explained. Figure 8(b) shows that the tyre load F_{tz1} increases when λ_{Af} increases.

4.1.4. Damping Valves. Figure 9 shows the influence of the damping coefficients of R_{g1}/R_{g2} on vehicle responses. It can be seen from Figures 9(a) and 9(b) that the damping coefficients have barely affected the peak values of vehicle responses. The reason for this phenomenon is that the fluid flowing through the damper valves at R_{g1}/R_{g2} runs at such low speeds so that the flow quantity can hardly contribute to the damping effects.

Based on the analyses above, the influences of physical parameters on vehicle handling performance can be concluded. In order to identify the most crucial factor for hydraulic suspension subsystems, the amplitude variations relative to physical parameters from Figures 6–9 are all summarized in Figure 10, where function $g(x) = |x_{max} - x_{min}|$. It is observed obviously that ΔA_f is the factor that affects the handling performance when compared with the other three

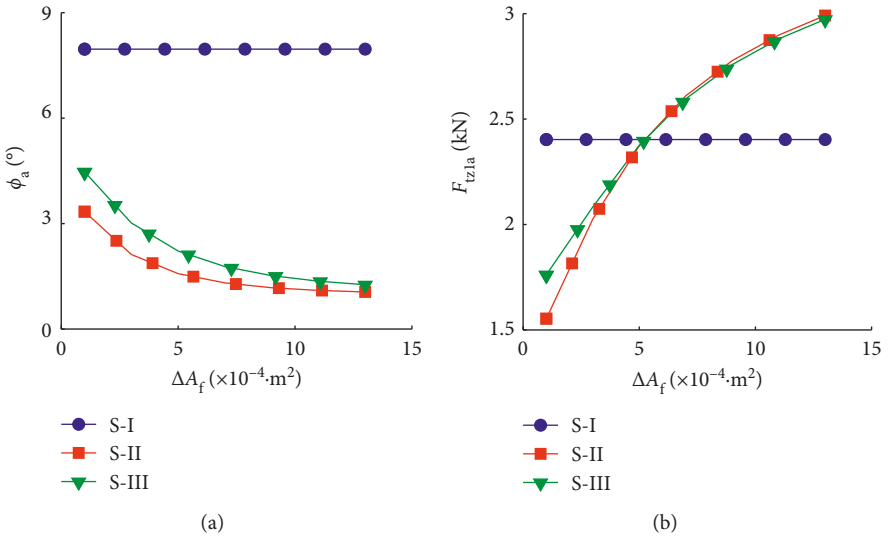

Figure 7: Influence of ΔA_f on amplitudes of vehicle responses: (a) roll angle of sprung mass; (b) vertical tyre force at left-front station.

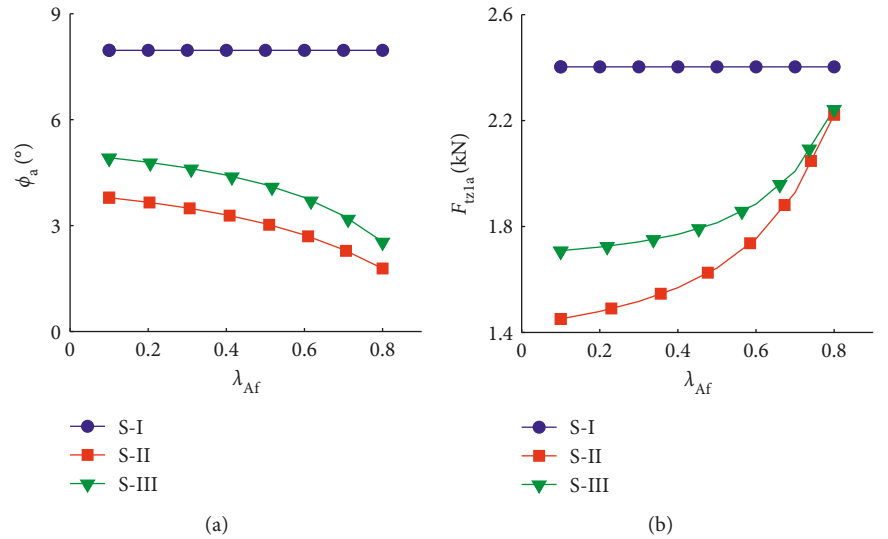

Figure 8: Influence of λ_{Af} on amplitudes of vehicle responses: (a) roll angle of sprung mass; (b) vertical tyre force at left-front station.

factors, which means that ΔA_f is the most crucial factor in DHIS subsystem for handling performance.

4.2. Influence of Physical Parameters on Ride Performance. According to ISO 2631-1997, responses of vehicle running on random road pavements are utilized to obtain the ride performance. A C-class level road pavement, corresponding to the road roughness coefficient $G_q(n_0) = 256 \times 10^{-6}$ m^3, is chosen as the road excitations of the tyres. The vehicle speed is still $v = 50$ km/h. In order to qualify the ride comfort effectively and thoroughly, three types of excitation methods, including the pure-bounce motion (the excitations on four tyres are of the same value and direction), pure-roll motion (the excitations on left and right tyres are of the same value but of the opposite directions), and pure-pitch motion (the excitations on front and rear tyres are of the same value but the opposite directions), are introduced to derive vehicle responses. Considering the defects of the time domain responses, such as the difficulty to obtain a smooth frequency spectrum in spite of road pavement errors [36], the frequency-domain response based on the power spectrum density (PSD) is utilized to evaluate the vehicle performance.

According to ISO 2631-1997, the weighted root mean square (WRMS) of accelerations at CG, denoted as σ_{aw}, is applied to evaluate the ride comfort, that is,

$$\sigma_{aw} = \left[\sum_{i=x,y,z} k_i \int_{\omega_l \le \omega \le \omega_u} w_i^2 S(a_i, \omega) d\omega \right]^{0.5}, \quad (22)$$

where k_i $(i = x, y, z)$ are the weighting factors in x-, y-, and z-axis; w_i $(i = x, y, z)$ are the frequency weighting factors along x-, y-, and z-axis; a_i $(i = x, y, z)$ are the accelerations at

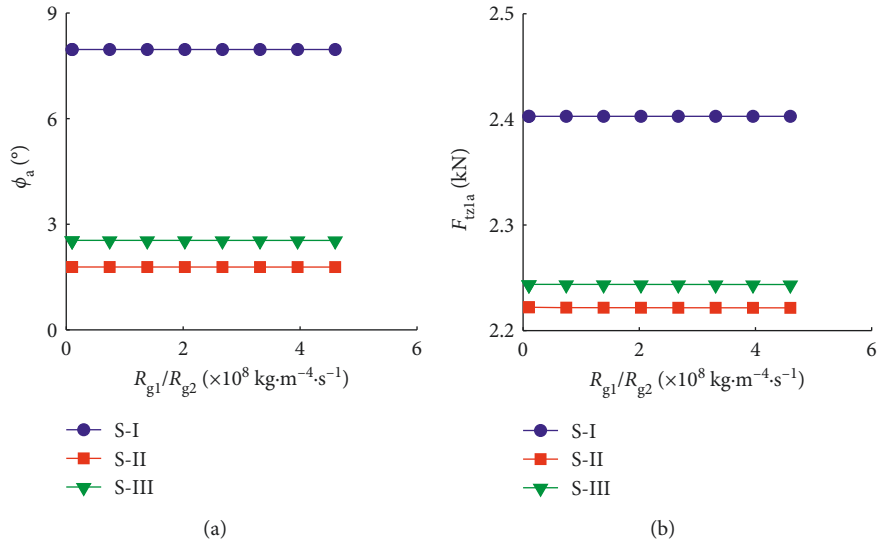

Figure 9: Influence of R_{g1}/R_{g2} on amplitudes of vehicle responses: (a) roll angle of sprung mass; (b) vertical tyre force at left-front station.

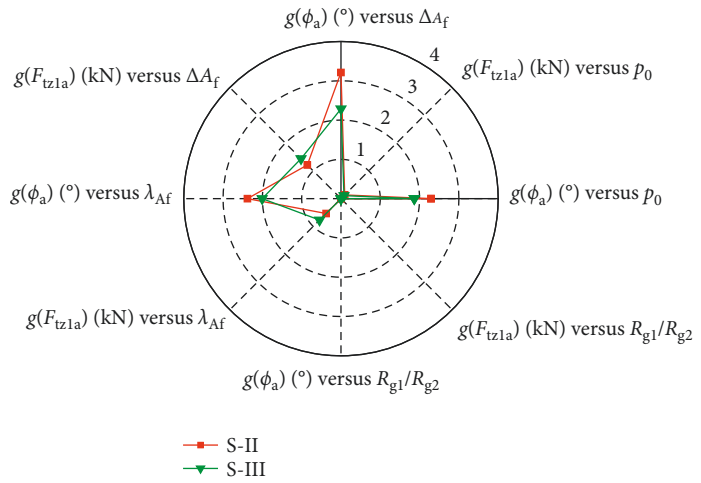

Figure 10: The influence of physical parameters on vehicle responses.

CG; $S(x, \omega)$ is the PSD value of x; and ω_l and ω_u are the lower and upper bounds of ω, respectively.

4.2.1. Precharged Oil Pressure. Figures 11(a)–11(c) depict the influence of precharged oil pressure p_0 on vehicle ride performance. In Figure 11(a), the ride comfort indicator σ_{aw} is slightly increased in pure-bounce when p_0 rises. In Figure 11(b), the indicator σ_{aw} has been observed a considerable increase for hydraulic suspension subsystems in pure-roll motion, which means the ride comfort has been deteriorated by the DHIS and HIS subsystems. However, the DHIS subsystem has a large advantage over HIS subsystem. Figure 11(c) shows that p_0 has negligible effect on σ_{aw}.

4.2.2. Area Difference in Front Hydraulic Cylinders. Figures 11(d)–11(f) depict the influence of the area difference ΔA_f on vehicle ride performance. Figure 11(d) has witnessed an upward trend of σ_{aw} in pure-bounce motion for hydraulic suspension subsystems when ΔA_f goes up. Figure 11(e) shows a similar trend of σ_{aw} in pure-roll motion as that in Figure 11(b), but the former undergoes much worse situations of ride performance than the latter. Figure 11(f) shows that the indicator σ_{aw} in pure-pitch motion has an optimal point where σ_{aw} is minimized for DHIS and HIS subsystems, respectively. But when ΔA_f goes up after that point, the ride comfort is worsened dramatically for both hydraulic suspension subsystems.

4.2.3. Area Ratio in Front Hydraulic Cylinders. Figures 12(a)–12(c) show the influence of area ratio λ_{Af} on ride comfort. Figure 12(a) shows that λ_{Af} has merely affected the ride comfort in pure-bounce motion when λ_{Af} is less than 0.5 for both hydraulic suspension subsystems. Figure 12(b)

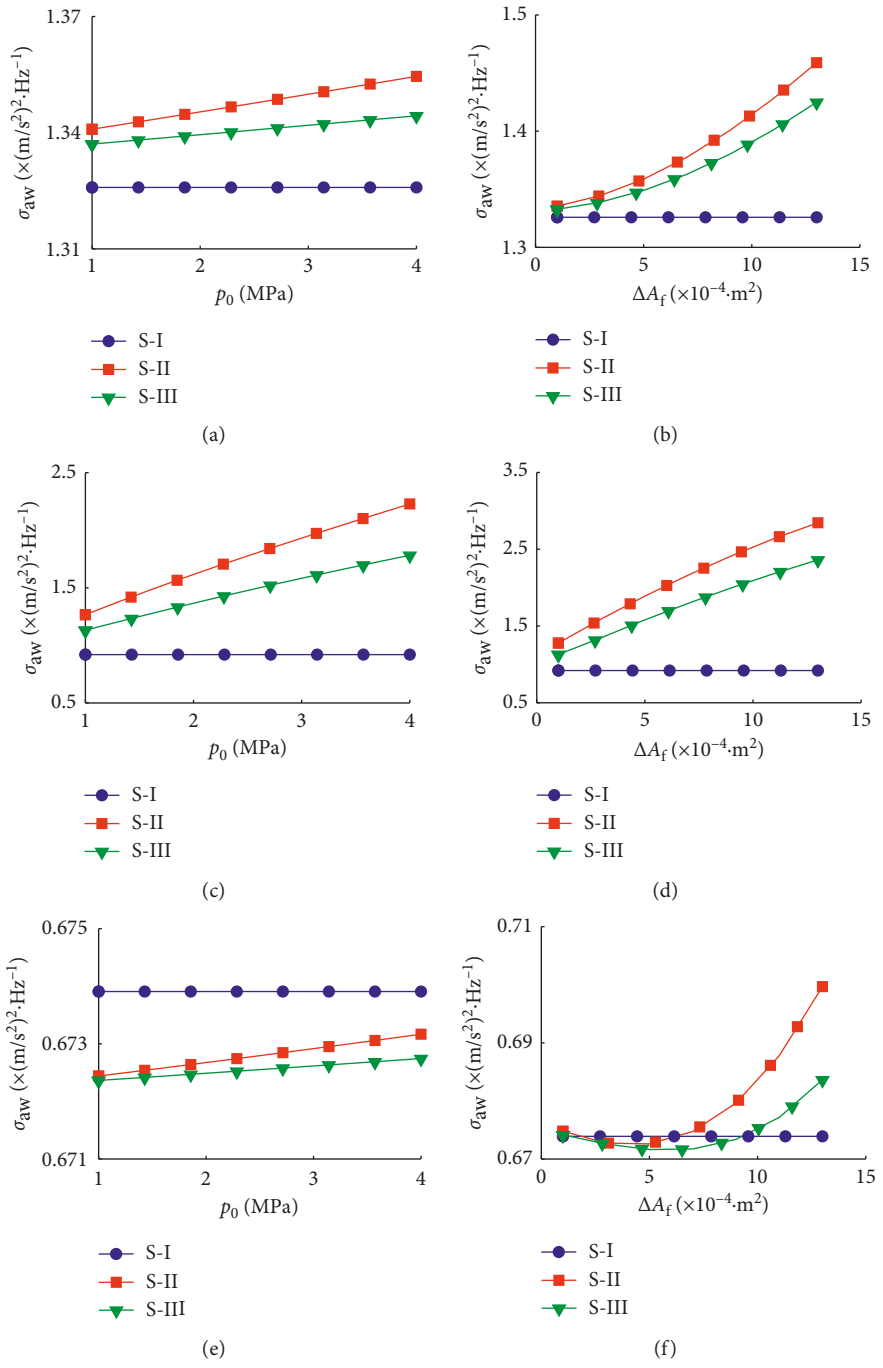

FIGURE 11: Influence of p_0 and ΔA_f on ride comfort indicator σ_{aw} in three motion modes: (a, d) in pure-bounce motion; (b, e) in pure-roll motion; (c, f) in pure-pitch motion.

shows that the ride comfort has been obviously damaged in pure-roll motion when λ_{Af} is larger than 0.6. Figure 12(c) shows that λ_{Af} has a trivial effect on σ_{aw}.

4.2.4. Damping Valves. Figures 12(d)–12(f) show the influence of area ratio λ_{Af} on ride comfort. Figure 12(d) shows that DHIS subsystem has little influence on ride comfort comparing with HIS subsystem when R_{g1}/R_{g2} changes in pure-bounce motion. Figure 12(e) shows that there exists an optimal point for DHIS subsystem to minimize σ_{aw}, while a downward trend of σ_{aw} can be witnessed for HIS subsystems. Figure 12(f) shows that the R_{g1}/R_{g2} has merely affected the ride comfort in pure-pitch motion.

Based on the analyses above, it is obvious that the four physical parameters play important roles in improving vehicle ride comfort. In order to identify the most crucial factor for the mechanical design of DHIS subsystem, the deviation of σ_{aw}, denoted by $g(\sigma_{aw})$, is applied to evaluate the

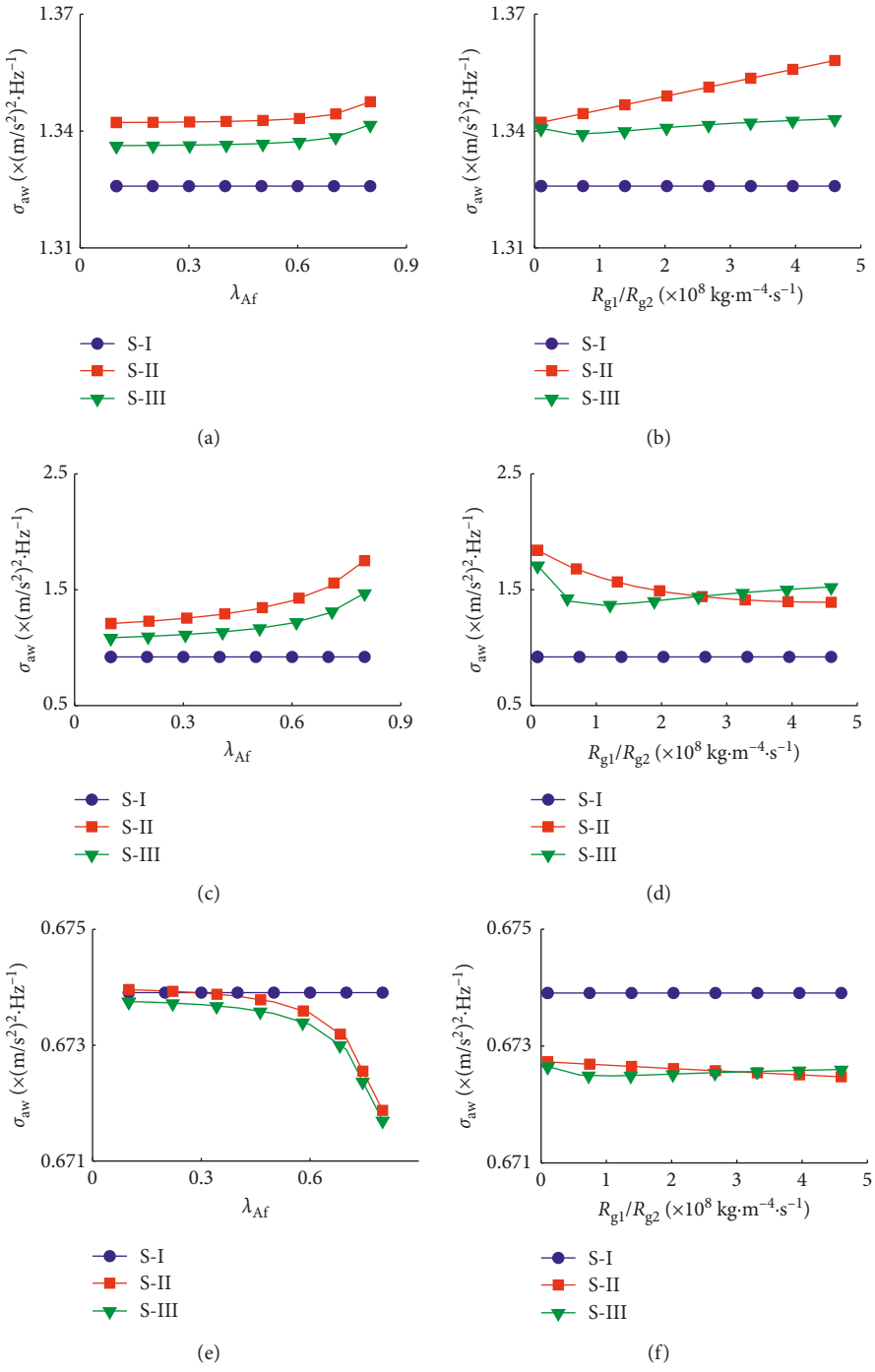

FIGURE 12: Influence of λ_{Af} and R_{g1}/R_{g2} on ride comfort indicator σ_{aw} in three motion modes: (a, d) in pure-bounce motion; (b, e) in pure-roll motion; (c, f) in pure-pitch motion.

perturbation of ride comfort when the physical parameters vary in the prescribed ranges. The results are shown in Figure 13, in which the data are generated with the results in Figures 11 and 12. From Figures 13(a)–13(c), we know that the area difference ΔA_f plays the most crucial role in ride performance of vehicle with hydraulic suspension subsystems, followed by precharged oil pressure λ_{Af} and p_0. On the other hand, the DHIS subsystem has narrower perturbation ranges on ride comfort than HIS subsystem, which means the DHIS subsystem can be used to provide a more comfortable experience for occupants than HIS subsystem.

4.3. Discussion. There still exist some deficiencies in this paper. For the first, the damping effect of the DHIS subsystem, including pipe damping and cylinder damping, is embodied into the valve damping effect. This simplification can effectively

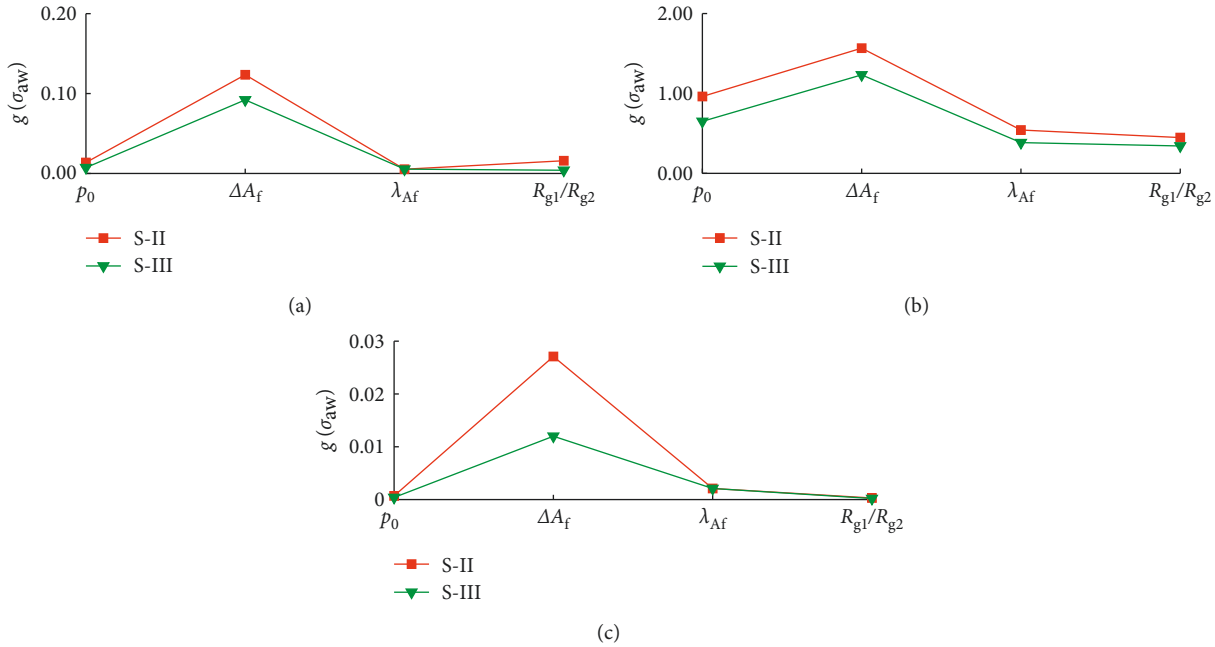

Figure 13: Influence of the physical parameters on the deviations of σ_{aw} in (a) pure-bounce motion; (b) pure-roll motion; (c) pure-pitch motion.

reduce the modeling complexity but may introduce some inaccuracies. Secondly, the leakage between chambers separated with rubber seal ring has been neglected, which may also contribute a lot to modal parameters shifting if fluid leakage emerges. Though it still presents challenges for modeling, but with the help of high-quality seal rings, these problems can be avoided effectively. Thirdly, as the discussions on damper valves R_{vi} are similar to that on R_{gi}, the investigation on R_{vi} is not presented for brevity. Meanwhile, the discussions of the feasible regions for these parameters will need to be further studied.

5. Conclusions

This paper generally presents a new type of hydraulically interconnected suspension system with dual accumulators at each fluid circuit. A 10-DOFs vehicle model coupled with DHIS subsystem is proposed and verified with results generated from MATLAB and CarSim software. Four crucial parameters of DHIS subsystem are chosen and assumed to vary in certain ranges. Thereafter, vehicle responses in time domain including roll angle and vertical tyre force, as well as responses in frequency domain in three types of road pavement excitations, are obtained for vehicles with three types of suspension subsystem. The main results are listed as follows:

(1) The simulation results of the proposed 10-DOFs vehicle model with DHIS subsystem fit well enough with those results acquired from CarSim software. It means that the 10-DOFs vehicle model can be used for further analyses.

(2) Four key physical parameters, including precharged oil pressure p_0, damping coefficients of R_{g1}/R_{g2}, chamber area difference ΔA_f, and ratio λ_{Af} in front axle, are taken to investigate their relationships with vehicle responses. Results show that the increases of p_0, ΔA_f, and λ_{Af} can restrain the roll propensity of vehicle body, while p_0 and λ_{Af} can help improve road holding, comparing with ΔA_f which could further deteriorate this capacity after a critical value. Meanwhile, the damping coefficients at R_{g1}/R_{g2} have negligible effects on both roll angle and tyre force. On the other hand, the four parameters can effectively affect the ride comfort in roll motion but have little effect on bounce and pitch motions.

(3) Results have shown that ΔA_f is the most crucial factor for both handling performance and ride comfort comparing with the other three factors, followed by λ_{Af} and p_0.

(4) DHIS subsystem can effectively enhance the roll-resistant property of vehicle comparing with the original spring-damper suspension system, and it can also benefit much to ride performance comparing with the conventional HIS subsystem.

Data Availability

The data used to support the findings of this study are available from the corresponding author upon request.

Conflicts of Interest

The authors declare that no conflicts of interest exist regarding the publication of this paper.

Acknowledgments

This work was supported by the National Natural Science Foundation of China (Grant no. 51675152) and Hunan Provincial Science Foundation of China (Grant no. 2017JJ2031).

References

[1] S. Kilicaslan, "Control of active suspension system considering nonlinear actuator dynamics," *Nonlinear Dynamics*, vol. 91, no. 2, pp. 1383–1394, 2018.

[2] Y. Wang, F. Kang, T. Wang, and H. Ren, "A robust control method for lateral stability control of in-wheel motored electric vehicle based on sideslip angle observer," *Shock and Vibration*, vol. 2018, Article ID 8197941, 11 pages, 2018.

[3] S. Wen, M. Z. Q. Chen, Z. Zeng, X. Yu, and T. Huang, "Fuzzy control for uncertain vehicle active suspension systems via dynamic sliding-mode approach," *IEEE Transactions on Systems Man Cybernetics-Systems*, vol. 47, no. 1, pp. 24–32, 2017.

[4] C. Li, H. Jing, R. Wang, and N. Chen, "Vehicle lateral motion regulation under unreliable communication links based on robust H_∞ output-feedback control schema," *Mechanical Systems and Signal Processing*, vol. 104, pp. 171–187, 2018.

[5] J. Zhang, W. Sun, and Z. Feng, "Vehicle yaw stability control via H_∞ gain scheduling," *Mechanical Systems and Signal Processing*, vol. 106, pp. 62–75, 2018.

[6] H. Yazici and M. Sever, "L_2 gain state derivative feedback control of uncertain vehicle suspension systems," *Journal of Vibration and Control*, vol. 2017, pp. 1–16, 2017.

[7] X. Tang, H. Du, S. Sun, D. Ning, Z. Xing, and W. Li, "Takagi-Sugeno fuzzy control for semi-active vehicle suspension with a magnetorheological damper and experimental validation," *IEEE-ASME Transactions on Mechatronics*, vol. 22, no. 1, pp. 291–300, 2017.

[8] S.-A. Chen, J.-C. Wang, M. Yao, and Y.-B. Kim, "Improved optimal sliding mode control for a non-linear vehicle active suspension system," *Journal of Sound and Vibration*, vol. 395, pp. 1–25, 2017.

[9] H. Li, J. Yu, C. Hilton, and H. Liu, "Adaptive sliding-mode control for nonlinear active suspension vehicle systems using T-S fuzzy approach," *IEEE Transactions on Industrial Electronics*, vol. 60, no. 8, pp. 3328–3338, 2013.

[10] B. L. Boada, M. J. L. Boada, L. Vargas-Melendez, and V. Diaz, "A robust observer based on H_∞ filtering with parameter uncertainties combined with neural networks for estimation of vehicle roll angle," *Mechanical Systems and Signal Processing*, vol. 99, pp. 611–623, 2018.

[11] W. Sun, Z. Zhao, and H. Gao, "Saturated adaptive robust control for active suspension systems," *IEEE Transactions on Industrial Electronics*, vol. 60, no. 9, pp. 3889–3896, 2013.

[12] C. Hung-Yi and H. Shiuh-Jer, "A new model-free adaptive sliding controller for active suspension system," *International Journal of Systems Science*, vol. 39, no. 1, pp. 57–69, 2008.

[13] P. Brezas, M. C. Smith, and W. Hoult, "A clipped-optimal control algorithm for semi-active vehicle suspensions: theory and experimental evaluation," *Automatica*, vol. 53, pp. 188–194, 2015.

[14] D. Hao, C. Zhao, and Y. Huang, "A reduced-order model for active suppression control of vehicle longitudinal low-frequency vibration," *Shock and Vibration*, vol. 2018, Article ID 5731347, 22 pages, 2018.

[15] J. Zhao, P. K. Wong, Z. Xie, X. Ma, and C. Wei, "Design of a road friendly SAS system for heavy-duty vehicles based on a fuzzy-hybrid-add and GH-control strategy," *Shock and Vibration*, vol. 2016, Article ID 6321765, 7 pages, 2016.

[16] J. Liu, X. Li, Z. Wang, and Y. Zhang, "Modelling and experimental study on active energy-regenerative suspension structure with variable universe fuzzy PD control," *Shock and Vibration*, vol. 2016, Article ID 6170275, 11 pages, 2016.

[17] D. Cao, S. Rakheja, and C.-Y. Su, "Roll- and pitch-plane coupled hydro-pneumatic suspension. Part 1: feasibility analysis and suspension properties," *Vehicle System Dynamics*, vol. 48, no. 3, pp. 361–386, 2010.

[18] A. J. Nieto, A. L. Morales, A. Gonzalez, J. M. Chicharro, and P. Pintado, "An analytical model of pneumatic suspensions based on an experimental characterization," *Journal of Sound and Vibration*, vol. 313, no. 1-2, pp. 290–307, 2008.

[19] A. E. Moulton and A. Best, "Rubber springs and interconnected suspension systems," in *Proceedings of the Engineering Design Show Conference*, Chicago, IL, USA, 1970.

[20] J. Félez and C. Vera, "Bond graph assisted models for hydro pneumatic suspensions in crane vehicles," *Vehicle System Dynamics*, vol. 16, no. 5-6, pp. 313–332, 1987.

[21] S. M. El-Demerdash and D. A. Crolla, "Hydro-pneumatic slow-active suspension with preview control," *Vehicle System Dynamics*, vol. 25, no. 5, pp. 369–86, 1996.

[22] P. S. Els and B. Grobbelaar, "Heat transfer effects on hydropneumatic suspension systems," *Journal of Terramechanics*, vol. 36, no. 4, pp. 197–205, 1999.

[23] A. R. Schumann and R. J. Anderson, "Optimal control of an active anti roll suspension for an off road utility vehicle using interconnected hydragas suspension units," *Vehicle System Dynamics*, vol. 37, pp. 145–156, 2002.

[24] S. Sridhar and N. S. Sekar, "Optimisation of kinematics for tracked vehicle hydro gas suspension system," *Defence Science Journal*, vol. 56, no. 5, pp. 753–768, 2006.

[25] U. Solomon and C. Padmanabhan, "Semi-active hydro-gas suspension system for a tracked vehicle," *Journal of Terramechanics*, vol. 48, no. 3, pp. 225–239, 2011.

[26] U. Solomon and C. Padmanabhan, "Hydro-gas suspension system for a tracked vehicle: modeling and analysis," *Journal of Terramechanics*, vol. 48, no. 2, pp. 125–137, 2011.

[27] D. Cao, S. Rakheja, and C.-Y. Su, "Roll plane analysis of a hydro pneumatic suspension with twin gas chamber struts," *International Journal of Heavy Vehicle Systems*, vol. 14, no. 4, pp. 355–375, 2007.

[28] D. Cao, S. Rakheja, and C.-Y. Su, "Dynamic analyses of roll plane interconnected hydro-pneumatic suspension systems," *International Journal of Vehicle Design*, vol. 47, no. 1–4, pp. 51–80, 2008.

[29] D. Cao, S. Rakheja, and C.-Y. Su, "Roll- and pitch-plane-coupled hydro-pneumatic suspension. Part 2: dynamic response analyses," *Vehicle System Dynamics*, vol. 48, no. 4, pp. 507–528, 2010.

[30] N. Zhang, W. A. Smith, and J. Jeyakumaran, "Hydraulically interconnected vehicle suspension: background and modelling," *Vehicle System Dynamics*, vol. 48, no. 1, pp. 17–40, 2010.

[31] F. Ding, X. Han, Z. Luo, and N. Zhang, "Modelling and characteristic analysis of tri-axle trucks with hydraulically interconnected suspensions," *Vehicle System Dynamics*, vol. 50, no. 12, pp. 1877–1904, 2012.

[32] N. Zhang, L. Wang, and H. Du, "Motion-mode energy method for vehicle dynamics analysis and control," *Vehicle System Dynamics*, vol. 52, no. 1, pp. 1–25, 2014.

[33] F. Ding, X. Han, N. Zhang, and Z. Luo, "Characteristic analysis of pitch resistant hydraulically interconnected suspensions for two axle vehicles," *Journal of Vibration and Control*, vol. 21, no. 16, pp. 3167–3188, 2014.

[34] J. Liang, J. Wu, N. Zhang, Z. Luo, and S. Zhu, "Interval uncertain analysis of active hydraulically interconnected suspension system," *Advances in Mechanical Engineering*, vol. 8, no. 5, article 168781401664633, 2016.

[35] B. Zhang, H. Du, J. Lam, N. Zhang, and W. Li, "A novel observer design for simultaneous estimation of vehicle steering angle and sideslip angle," *IEEE Transactions on Industrial Electronics*, vol. 63, no. 7, pp. 4357–4366, 2016.

[36] X. Liu, H. Wang, Y. Shan, and T. He, "Construction of road roughness in left and right wheel paths based on PSD and coherence function," *Mechanical Systems and Signal Processing*, vol. 60-61, pp. 668–677, 2015.